Chemical Science

EDGE ARTICLE

View Article Online
View Journal | View Issue

Check for updates

Cite this: *Chem. Sci.*, 2026, **17**, 274

All publication charges for this article have been paid for by the Royal Society of Chemistry

Received 27th August 2025
Accepted 29th October 2025

DOI: 10.1039/d5sc06565h

rsc.li/chemical-science

Phenphosphine-X(O, S, Se) locking multi-resonance thermally activated delayed fluorescence materials

Xian-Fang Hong, Yi Wei, Hao-Ran Xing, Yu Wang, Jia-Qi Xi, Chen-Yang Wu, Li Yuan,* Cheng-Hui Li and You-Xuan Zheng*

Multi-resonance thermally activated delayed fluorescence (MR-TADF) materials with narrowband emission and high efficiency are crucial for achieving ultra-high-definition displays. However, organic light-emitting diodes (OLEDs) based on MR-TADF emitters suffer from severe efficiency roll-off. Herein, we employ a phenphosphine-X(O, S, Se) locking strategy with heavy atoms to accelerate the reverse intersystem crossing (RISC) process. Three emitters NBNPO, NBNPS, and NBNPSe exhibit blue emission peaking at 468–471 nm with a full-width at half-maximum of 19 nm (0.11 eV) in toluene. The doped films show photoluminescence efficiencies of up to 95% with RISC rate constants as high as 5.92×10^4, 4.62×10^5, and 9.91×10^6 s^{-1} for NBNPO, NBNPS, and NBNPSe, respectively. The corresponding OLEDs achieve maximum external quantum efficiencies of up to 32.4% with gradually decreased efficiency roll-off. These findings highlight a promising molecular design strategy for efficient MR-TADF materials and OLEDs.

Introduction

Luminescent materials with high efficiency and excellent color purity are essential for organic light-emitting diodes (OLEDs) toward ultra-high-definition displays. In general, fluorescent, phosphorescent, and thermally activated delayed fluorescence (TADF) molecules with conventional donor–acceptor structures always show broad emission spectra because of structural deformation in the excited state and the molecular vibrations. To resolve this problem, in 2016, Hatakeyama *et al.* introduced a pioneering molecular design strategy for multi-resonance TADF (MR-TADF) emitters.[1] By alternately incorporating electron-deficient boron and electron-rich nitrogen atoms into a rigid polycyclic aromatic hydrocarbon framework, spatial separation of the highest occupied molecular orbital (HOMO) and lowest unoccupied molecular orbital (LUMO) through opposing resonance effects was achieved. This unique molecular architecture effectively suppresses vibrational coupling, minimizes structural relaxation, and enables narrowband emission with a full width at half-maximum (FWHM) of less than 40 nm.

Over the past decade, a wide range of MR-TADF emitters have been extensively investigated.[2–5] Among the reported MR-TADF scaffolds, DtCzB (Fig. 1) has attracted particular attention due to its structural simplicity and tunability.[6–8] Structural modification of the DtCzB molecule has enabled emission wavelength tuning,[9–12] and enhanced device performance.[13–15] However, asymmetric or uncontrolled π-conjugation extension often limits the ability to modulate the energy gap and disrupts the MR effect, resulting in significantly weakened or even lost TADF behavior.[16–18] Furthermore, the introduction of strong donor/acceptor groups may reduce molecular rigidity and enhance vibronic coupling between ground and excited states, thereby broadening the emission spectrum.[19,20]

To overcome the aforementioned challenges, recent studies have introduced functional heteroatoms at the C_1 and C_2 positions (Fig. 1) of the DtCzB core to precisely regulate emission properties while preserving molecular rigidity and MR-TADF characteristics, thereby achieving a synergy between functionality and efficiency. This approach is referred to as the molecular "locking" design strategy. In 2022, Zhang *et al.* reported a spiro-locking strategy that enhanced molecular planarity and reduced excited-state structural distortion (CzphB-FI) by suppressing intramolecular charge transfer (ICT), resulting in narrowband green emission and a maximum external quantum efficiency (EQE_{max}) of up to 31% in the device.[21] In 2023, Duan *et al.* introduced a tris(*m*-methylphenyl) borane locking unit in DBCz-Mes to alleviate intramolecular steric hindrance, achieving ultra-pure blue emission (FWHM = 14 nm, CIE = (0.144, 0.042)) and an EQE_{max} of 33.9% in OLEDs.[22] Subsequently, Wang *et al.* incorporated electron-rich sulfur (S) atoms and a spiro-carbon locking motif into the DtCzB framework to construct FSBN, S-BN, and 2S-BN derivatives, successfully realizing efficient red and near-infrared emission.[23,24] These studies demonstrate that the locking molecular design strategy and the introduction of heteroatoms with distinct functionalities can endow materials with desirable properties.

State Key Laboratory of Coordination Chemistry, Jiangsu Key Laboratory of Advanced Organic Materials, School of Chemistry and Chemical Engineering, Nanjing University, Nanjing 210023, P. R. China. E-mail: yxzheng@nju.edu.cn; yl@nju.edu.cn

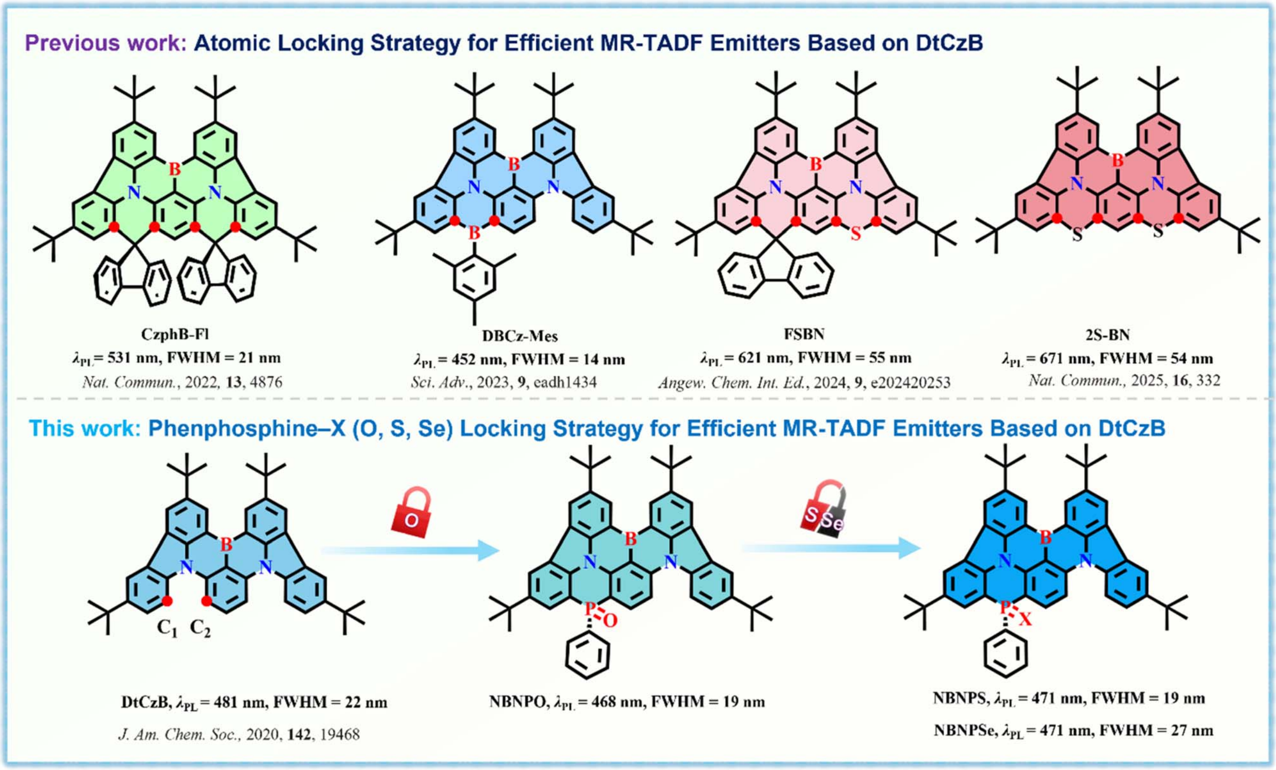

Fig. 1 Atomic locking molecular design strategy for the MR-TADF materials based on the DtCzB core reported previously and in this work.

In general, MR-TADF emitters usually possess long delay lifetimes and low reverse intersystem crossing (RISC) rate constants (k_{RISC}), which lead to serious device efficiency roll-off at high brightness. According to Fermi's golden rule, improving the spin–orbit coupling (SOC) can accelerate the RISC process. By introducing the functional units and heteroatoms, the SOC effect of the corresponding MR-TADF materials can be enhanced to relieve their device efficiency roll-off. For example, the P═O unit, which possesses moderate electron-withdrawing ability and good electron-transport characteristics, has been introduced as a functional group in MR-TADF materials to enhance their optoelectronic properties.[25–28] In 2022, Xu *et al.* integrated the ambipolar P═O host segment into an MR-TADF molecule, simultaneously accelerating singlet (S_1) radiation and suppressing both S_1 and triplet (T_1) nonradiative losses.[29] Zhang *et al.* incorporated the P═O unit to modify the DtCzB molecule, significantly accelerating the RISC process while retaining the narrowband emission characteristics.[30] Additionally, the heavy-atom effect has also been verified to be an effective method to accelerate the RISC process. For instance, Yasuda *et al.* introduced S and selenium (Se) into MR-TADF emitters,[31] realizing a quasi-single-component emission with k_{RISC} values exceeding 10^8 s^{-1}. Subsequently, Yang *et al.* reported a Se-integrated B/N skeleton with a high kRISC of 2.0×10^6 s^{-1} and low device efficiency roll-off.[32] Based on these results, it is speculated the simultaneous introduction of P═O groups and heavy atoms into MR-TADF molecules is hopefully further improve their properties.

Herein, we employed a phenphosphine–oxygen (Ph–P═O) locking molecular design strategy and replaced the O atom in the P═O moiety with S and Se to further accelerate the RISC process, affording three blue-emitting materials, NBNPO, NBNPS, and NBNPSe (Fig. 1). The pentavalent sp^3-hybridized phosphorus atom introduces substantial steric hindrance and conformational rigidity, promoting molecular twisting and suppressing aggregation-induced quenching.[33–35] In dilute toluene, these compounds exhibit emission maxima at 468, 471, and 471 nm with FWHMs of 19 (0.11 eV), 19 (0.11 eV), and 27 nm (0.15 eV), respectively. In doped films, the k_{RISC}s are calculated to be 5.92×10^4, 4.62×10^5, and 9.91×10^6 s^{-1} for NBNPO, NBNPS, and NBNPSe, respectively. Accordingly, the OLEDs achieve EQE_{max}s of 32.4%, 31.6%, and 11.4%, with FWHMs of 22 (0.13 eV), 27 (0.15 eV), and 33 nm (0.18 eV), respectively, and gradually decreased efficiency roll-off.

Results and discussion

Synthesis and single crystal analysis

The construction of NBNPX (X = O, S, Se) molecules comprises two main steps. Initially, the DtCzB core was synthesized *via* nucleophilic aromatic substitution between commercially available precursors and 3,6-di-*tert*-butylcarbazole, followed by a one-step borylation to yield the desired intermediate. In the second step, a phenphosphine oxide locking unit was introduced onto the DtCzB core, with further modification enabling the substitution of the O atom by S or Se. All intermediates and final products were unambiguously characterized by ^{1}H and ^{13}C NMR spectroscopy as well as high-resolution mass spectrometry (Fig. S1–S13). Thermogravimetric analysis curves display excellent thermal stability for the three materials, with 5 wt% weight-loss decomposition temperatures of 481 °C for NBNPO, 464 °C for NBNPS, and 445 °C for NBNPSe (Fig. S14), respectively, which are favorable for operation in their corresponding OLEDs. Cyclic voltammetry (Fig. S15) curves reveal the HOMO/LUMO energy levels of −5.41/−2.68 eV for NBNPO, −5.19/−2.49 eV for NBNPS, and −5.42/−2.73 eV for NBNPSe, respectively.

Single crystals of NBNPO, NBNPS, and NBNPSe were obtained by slow evaporation of toluene/methanol mixed solvents. Fig. 2b and c display the molecular structures and crystal packing patterns of NBNPO, NBNPS, and NBNPSe, respectively. As shown in Fig. 2b, all compounds feature a Ph–P═X locking unit, with P–C bond lengths increasing from 1.77/1.76 Å (NBNPO) to 1.79/1.79 Å (NBNPS) and 1.81/1.80 Å (NBNPSe), in line with the ascending atomic size of the heteroatoms (O, S, and Se). A similar trend is also observed for the P–X bonds, measured at 1.48 Å (P–O), 1.94 Å (P–S), and 2.10 Å (P–Se), respectively. These variations reflect distinct changes in the electronic environment surrounding the phosphorus center and correlate with the observed thermal stability and photophysical property differences. The Ph–P═X locking motif effectively reduces steric repulsion between adjacent hydrogen atoms, thereby enhancing molecular rigidity and planarity, suppressing nonradiative vibrational deactivation of the molecules.[27] Moreover, the phenyl rings and heteroatoms (O, S, and Se) on phosphorus are oriented on opposite sides of the molecule, introducing steric hindrance that mitigates aggregation in the solid state. As depicted in Fig. 2c, all three compounds adopt a head-to-tail packing arrangement, with heteroatoms oriented inward and phenyl rings facing outward. The π–π stacking distances increase from 3.45 Å (NBNPO) to 3.51 Å (NBNPS) and 3.66 Å (NBNPSe), which are beneficial for vacuum deposition and may help suppress exciton quenching in devices.

Theoretical calculations and photophysical properties

To understand how heteroatom substitution modulates the electronic structure in theory, we performed ground-state geometry optimizations for all three compounds using DFT at the B3LYP/6-31G(d,p) level. As shown in Fig. 3a, c and e, all molecules exhibit well-separated HOMO and LUMO distributions, favorable for MR-type short-range charge transfer (SRCT) transitions. Notably, the *meta*-positioning of the P═X units relative to the boron center exerts a pronounced influence on the HOMO distribution. As the heteroatom is varied from O to S and Se, a gradual increase in HOMO delocalization is observed along the molecular backbone, accompanied by a significant rise in heteroatomic contribution to the HOMO orbital. Time-dependent DFT (TD-DFT) calculations further reveal that all materials have rapid radiative decay processes and efficient TADF characteristics. To further elucidate the effect of heteroatoms on TADF performances, SOC matrix elements ($\langle S_1|\hat{H}_{SOC}|T_1\rangle$) between S_1 and T_1 states were calculated using the PySOC package.[32] As shown in Fig. 3b, d and f, the SOC values increase systematically with the atomic number of the

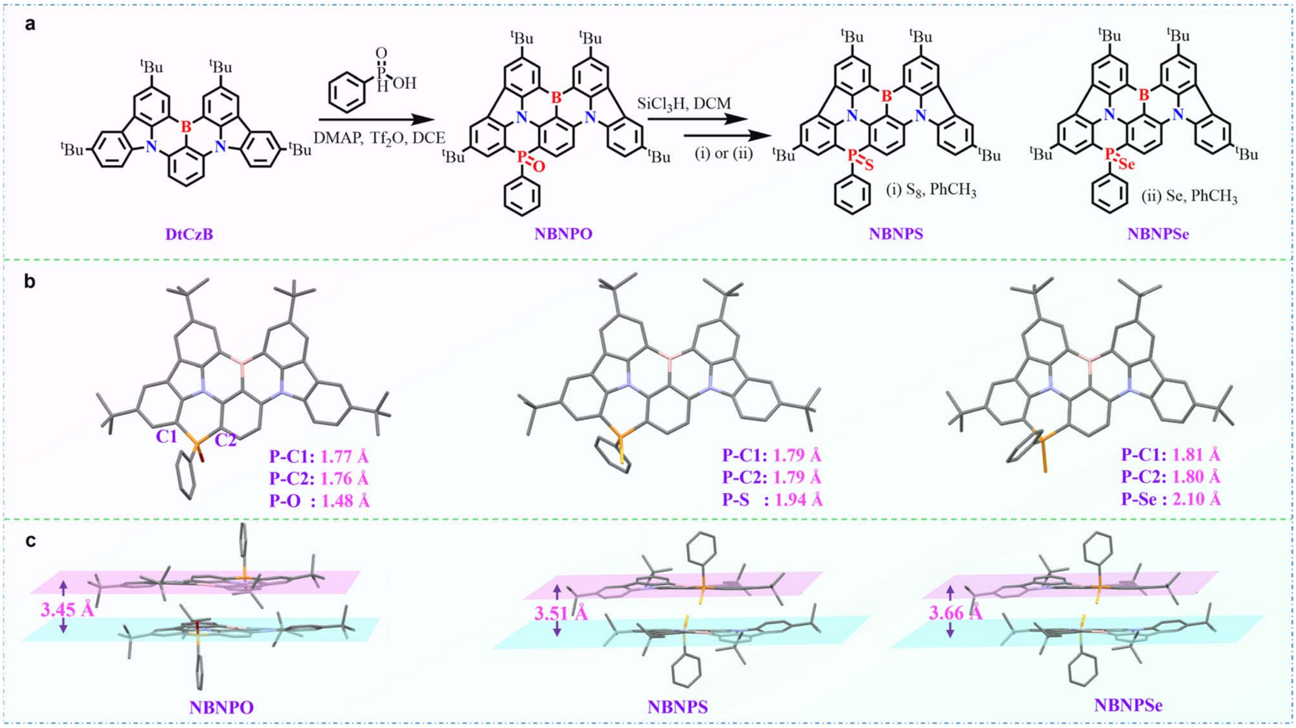

Fig. 2 (a) Synthetic route for target MR-TADF molecules. (b) Molecular structures of the target compounds in the crystal state. (c) Molecular packing modes of the target compounds in the crystal state.

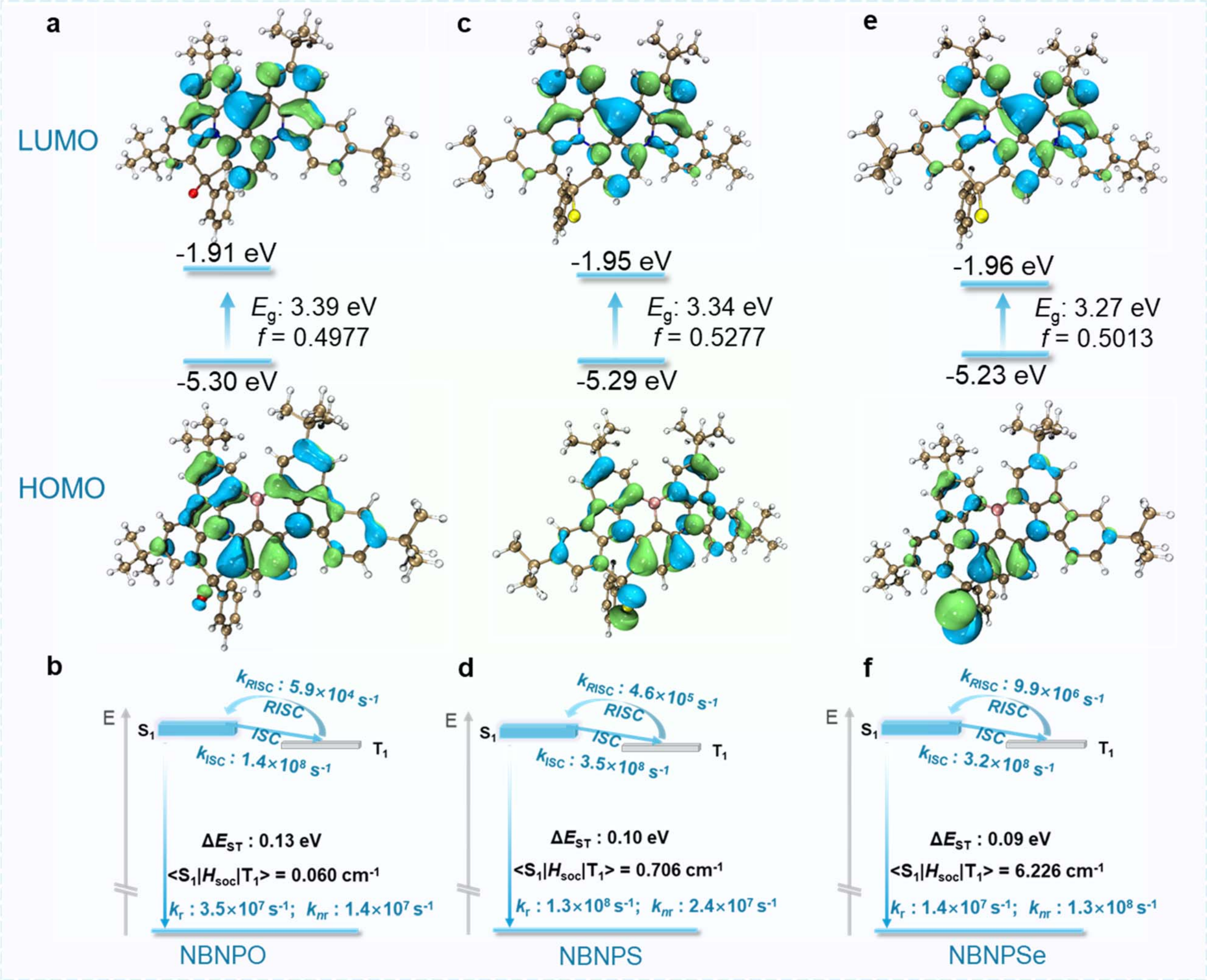

Fig. 3 Theoretical results of NBNPO, NBNPS, and NBNPSe: (a), (c), and (e) optimized molecular geometries, Kohn–Sham frontier orbital distributions, oscillator strengths, theoretical energy levels, and energy gaps. (b), (d), and (f) Energy level diagrams of singlet and triplet states, along with the SOC matrix elements calculated using PySOC and the ΔE_{ST} values corrected by the SCS-CC2 method.

heteroatoms: 0.060 cm^{-1} (NBNPO), 0.706 cm^{-1} (NBNPS), and 6.226 cm^{-1} (NBNPSe). The SCS-CC2-corrected ΔE_{ST} values of 0.13, 0.10, and 0.09 eV closely align with experimental data and fall within the optimal range for promoting efficient RISC. In theory, the combination of large SOC and small ΔE_{ST} values should facilitate accelerated RISC and thereby enhance emission efficiency.[36–39]

The photophysical properties of NBNPO, NBNPS, and NBNPSe in dilute toluene were systematically investigated (Fig. 4a–c). UV-visible absorption spectra exhibit a weak band below 380–390 nm, attributed to n–π* and π–π* electronic transitions, and sharp and intense bands at 455, 460, and 461 nm, respectively, belonging to the SRCT transition, a hallmark of MR systems. Upon excitation at 330 nm, all three compounds emit blue emission with peak maxima at 468 nm (NBNPO), 471 nm (NBNPS), and 471 nm (NBNPSe), and FWHMs of 19 (0.11 eV), 19 (0.11 eV), and 27 nm (0.15 eV), respectively. The corresponding CIE coordinates are (0.12, 0.10), (0.11, 0.12), and (0.13, 0.14), respectively, highlighting their excellent color purity. Notably, the photoluminescence (PL) spectra exhibit near-mirror symmetry with their absorption profiles, and the small Stokes shifts of 13 nm (NBNPO), 11 nm (NBNPS), and 10 nm (NBNPSe) suggest minimal geometric reorganization between the ground and excited states. These results confirm that the incorporation of the Ph–P═X locking units at the *meta*-position effectively restricts structural relaxation. To further elucidate the origin of spectral broadening of NBNPSe, the extent of geometric reorganization and reorganization energies of the three emitters was quantitatively analyzed. As shown in Fig. S22 and S23, the RMSD values between the S_0 and S_1 geometries are 0.200, 0.114, and 0.573 Å for NBNPO, NBNPS, and NBNPSe, respectively, with corresponding reorganization energies of 0.162, 0.152, and 0.249 eV. Notably, NBNPSe exhibits the largest structural relaxation and the highest reorganization energy after excitation, indicative of more significant vibronic coupling. The more pronounced geometric relaxation broadens the excited-state potential energy surface, thus rationally explaining the experimentally observed emission broadening

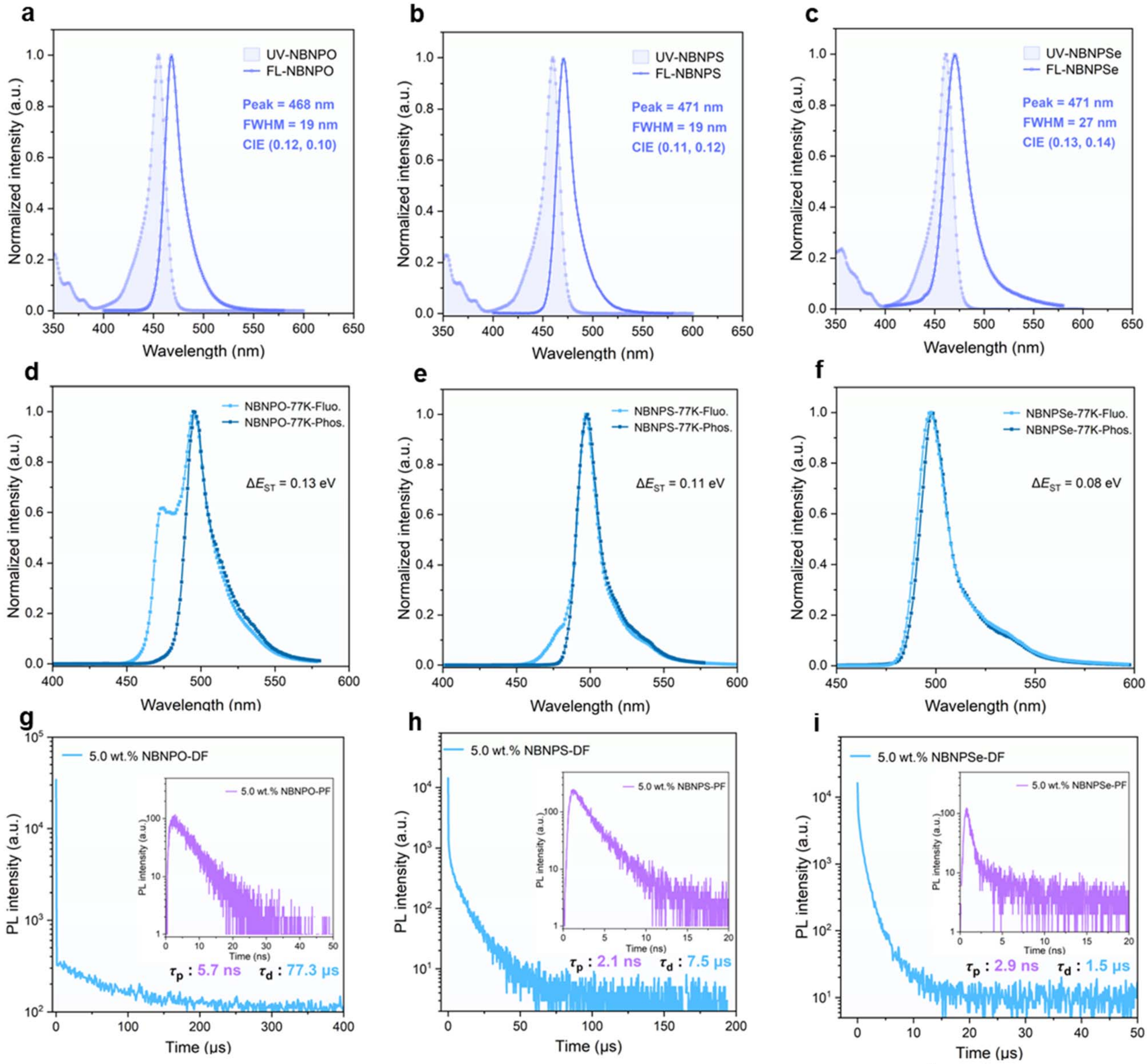

Fig. 4 Normalized UV-vis absorption and fluorescence spectra of (a) NBNPO, (b) NBNPS, and (c) NBNPSe in toluene (1.0×10^{-5} mol L^{-1}) at room temperature. Fluorescence and phosphorescence spectra of (d) NBNPO, (e) NBNPS, and (f) NBNPSe in toluene (1.0×10^{-5} mol L^{-1}) at 77 K. Prompt (inset) and delayed time-resolved photoluminescence decay curves of 5 wt% (g) NBNPO-, (h) NBNPS-, and (i) NBNPSe-doped films in mCBP at room temperature.

for NBNPSe. Additionally, from the fluorescence and phosphorescence spectra of NBNPO, NBNPS, and NBNPSe recorded at 77 K, the ΔE_{ST} values are determined to be 0.13, 0.11, and 0.08 eV, respectively (Fig. 3d–f), indicating the potential for efficient triplet harvesting of the three materials. Shoulder peaks corresponding to higher singlet excited states were observed in the PL spectra of NBNPO and NBNPS, potentially affecting ΔE_{ST} determination. Using temperature-dependent transient photoluminescence decay, ΔE_{ST} values were measured to be 0.15 and 0.09 eV, respectively (Fig. S20 and S21), in good agreement with the above measured results.

To further examine their solid-state photophysical characteristics, thin films with each emitter doped in a wide-bandgap host, 3,3′-di(9*H*-carbazolyl)biphenyl (mCBP) at a 5 wt% concentration, were fabricated (Fig. 4g–i and Table 1). The PL efficiencies (Φ_{PL}s) were determined to be 92%, 95%, and 61% for NBNPO, NBNPS, and NBNPSe, respectively. The PL decay curves reveal distinct differences of the three compounds. NBNPO exhibits a long delayed fluorescence lifetime (τ_{d}) of 77.3 µs, with a k_{RISC} of 5.92×10^4 s^{-1}, whereas S incorporation in NBNPS significantly shortens the τ_{d} to 7.45 µs, corresponding to a k_{RISC} of 4.62×10^5 s^{-1}. This result indicates that S incorporation in NBNPS effectively facilitates the RISC process *via* a moderate heavy atom effect while maintaining high Φ_{PL}. In contrast, further substitution with Se in NBNPSe resulted in a shorter τ_{d} of 1.48 µs and a much higher k_{RISC} of 9.91×10^6 s^{-1}.

Table 1 Photophysical data of relevant MR-TADF materials[l]

Compound	λ_{abs}[a] [nm]	λ_{PL}[b] [nm]	FWHM[c] [nm eV^{-1}]	Φ_{PL}[d] [%]	Φ_p[e] [%]	Φ_d[e] [%]	τ_p[f] [ns]	τ_d[f] [μs]	f[g]	k_r[h] [10^8 s^{-1}]	k_{ISC}[i] [10^8 s^{-1}]	k_{RISC}[j] [10^4 s^{-1}]	ΔE_{ST}[k] [eV]
NBNPO	455	468	19/0.11	92	21.40	78.60	5.66	77.3	0.50	0.348	1.42	5.92	0.13
NBNPS	460	471	19/0.11	95	28.51	71.49	2.06	7.45	0.53	1.31	3.53	46.2	0.11
NBNPSe	461	471	27/0.15	61	6.64	93.36	2.93	1.48	0.51	0.138	3.28	991	0.08

[a] Maximum absorption wavelength in toluene (1.0×10^{-5} mol L^{-1}). [b] Maximum emission wavelength in toluene (1.0×10^{-5} mol L^{-1}). [c] FWHM of the PL spectrum in toluene (1.0×10^{-5} mol L^{-1}). [d] Absolute PL efficiency measured using an integrating sphere. [e] Fractional PL efficiencies of prompt fluorescence (Φ_p) and delayed fluorescence (Φ_d); $\Phi_p + \Phi_d = \Phi_{PL}$. [f] Emission lifetimes of prompt (τ_p) and delayed (τ_d) fluorescence components. [g] Calculated oscillator strength for the $S_0 \rightarrow S_1$ transition. [h] Radiative decay rate constant of fluorescence ($S_1 \rightarrow S_0$, $k_r = \Phi_p/\tau_p$). [i] Rate constant of intersystem crossing ($S_1 \rightarrow T_1$, $k_{ISC} = (1 - \Phi_p)/\tau_p$). [j] Rate constant of reverse intersystem crossing ($T_1 \rightarrow S_1$, $k_{RISC} = \Phi_d/(k_{ISC} \cdot \tau_p \cdot \tau_d \cdot \Phi_p)$). [k] Singlet–triplet energy gap estimated from the λ_{PL} positions of fluorescence and phosphorescence spectra. [l] Data measured from the film prepared by doping 5 wt% NBNPX in the mCBP host.

Consistent with these observations, the radiative decay rates (k_r) also show pronounced variation: 3.48×10^7 s^{-1} for NBNPO, 1.31×10^8 s^{-1} for NBNPS, and a significantly lower value of 1.38×10^7 s^{-1} for NBNPSe.

Despite exhibiting both the largest SOC and smallest ΔE_{ST}, NBNPSe shows a markedly lower Φ_{PL} compared to that of NBNPS. According to Fermi's golden rule, the rate of electronic transitions depends on both the electronic coupling strength and the energy resonance. While the increased SOC and reduced ΔE_{ST} are favorable for RISC, the incorporation of heavy atoms can introduce competing nonradiative decay pathways.[40] For instance, stronger intramolecular vibrational coupling and pronounced excited-state geometric relaxation may elevate the nonradiative decay rate (k_{nr}). Due to the high polarizability and orbital diffuseness of the Se atom, NBNPSe is more susceptible to internal conversion (IC) and excited-state relaxation, resulting in higher energy dissipation.[41–43] Consequently, despite its favorable RISC characteristics, NBNPSe suffers from significant nonradiative losses that ultimately reduce Φ_{PL}. In contrast, NBNPS achieves a more optimal balance. Its moderately increased SOC (0.70 cm^{-1}) effectively supports the RISC process, while the small ΔE_{ST} (0.09 eV) helps to suppress internal conversion, leading to the highest Φ_{PL}. These findings underscore the importance of fine-tuning the heavy atom effect and simultaneously enhancing SOC and suppressing detrimental nonradiative decay mechanisms, such as vibrational coupling and excited-state relaxation, in the rational design of efficient TADF materials.

Electroluminescent properties

To evaluate the electroluminescence (EL) performances of these materials, OLEDs were fabricated using the configuration: ITO/HATCN (1,4,5,8,9,11-hexaazatripheny-lenehexacarbonitrile, 5 nm)/TAPC (*N*,*N*-bis(*p*-tolyl)aniline, 30 nm)/mCP (*N*,*N*-dicarbazolyl-3,5-benzene, 5 nm)/emissive layer (20 nm)/PPF (2,8-bis(diphenylphosphoryl)dibenzofuran, 5 nm)/BPhen (bathophenanthroline, 30 nm)/LiF (1 nm)/Al (100 nm). In this architecture, HATCN and TAPC serve as the hole injection and transport layers, LiF and BPhen act the electron injection and transport layers, and mCP and PPF play as exciton-blocking layers, respectively. The emissive layer employs the wide-bandgap host mCBP. Depending on the emitters, the devices are denoted as D-NBNPO, D-NBNPS, and D-NBNPSe, respectively. Devices (D′-NBNPO, D′-NBNPS, and D′-NBNPSe) were fabricated using NBNPO, NBNPS, and NBNPSe (3 wt%) as dopants in mCBP (Fig. S32 and Table S14). The D′-NBNPO exhibits blue EL peaking at 467 nm with a FWHM of 22 nm (0.13 eV) and an EQE$_{max}$ of 22.4%, but suffered a pronounced efficiency roll-off of 80% at 100 cd m^{-2}. In contrast, the introduction of heavy S and Se atoms endows NBNPS and NBNPSe with a larger k_{RISC}, effectively mitigating efficiency roll-off in their devices. The D′-NBNPS and D′-NBNPSe based devices show EL spectrum peaking at 470 and 471 nm with FWHMs of 26 (0.15 eV) and 32 nm (0.17 eV), and EQE$_{max}$s of 20.5% and 5.2%, with decreased efficiency roll-offs of 48% and 12% at 100 cd m^{-2}, respectively. Despite improved efficiency retention, the overall performances of both devices remain at a low level.

To improve device performance and suppress efficiency roll-off, a TADF sensitization strategy was employed to harvest triplet excitons *via* auxiliary pathways, thus compensating for the MR emitters with intrinsically low k_{RISC}.[44–46] Based on the absorption feature of NBNPO at around 455 nm, a series of TADF sensitizers emitting near this wavelength were screened. Among these, m4TCzPhBN emerged as the optimal sensitizer due to its favorable photophysical properties,[47] including a high T_1 energy (2.86 eV), a high k_{RISC} (1.0×10^6 s^{-1}), and nearly complete spectral overlap with the absorption of NBNPO (Fig. S33). This spectral alignment facilitates efficient Förster energy transfer, thereby improving sensitization efficiency and exciton utilization. The D-NBNPO, D-NBNPS and D-NBNPSe devices incorporating the TADF sensitization strategy show electroluminescence (EL) spectral peaking at 467, 472, and 472 nm with FWHMs of 22 (0.13 eV), 27 (0.15 eV), and 33 nm (0.18 eV) and CIE coordinates of (0.12, 0.09), (0.11, 0.12), and (0.12, 0.13) (Fig. 5), demonstrating good blue color purity. Compared with the PL spectra of the three emitters, the spectral shift is negligible. Furthermore, the change in EL spectra is ignorable as the drive voltage increases from 7 to 13 V, implying that these devices possess exceptional spectral stability (Fig. S35).

Additionally, all sensitized OLEDs exhibit good performances. For D-NBNPO, an EQE$_{max}$ of 32.4%, a maximum current efficiency (CE$_{max}$) of 34.6 cd A-1 and a maximum power efficiency (PE$_{max}$) of 25.9 lm W^{-1} were achieved. At a brightness of 100 cd m^{-2}, the EQE decreases to 17.6%, suggesting relatively

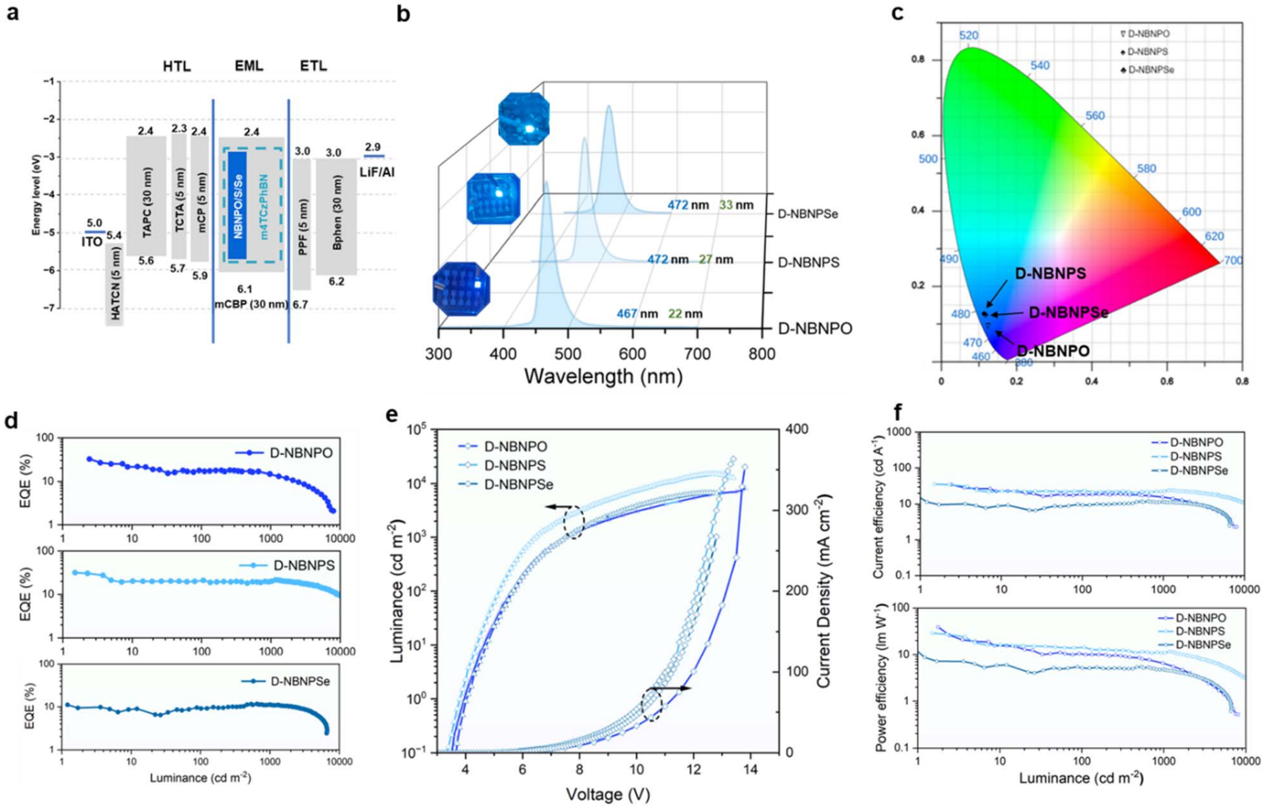

Fig. 5 (a) Device architecture and the corresponding energy-level diagram. (b) Electroluminescence spectra. (c) CIE chromaticity coordinates. (d) Current density/luminance *versus* driving voltage characteristics. (e) External quantum efficiency *versus* luminance curves. (f) Power efficiency and current efficiency *versus* luminance curves of D-NBNPO, D-NBNPS, and D-NBNPSe.

serious efficiency roll-off, partially due to the relatively long delayed lifetime (77.3 μs) of NBNPO. But at a high luminance of 1000 cd m^{-2}, the EQE can be kept at 14.7%, and the efficiency roll-off is alleviated, maybe due to the molecular rigidity caused by the Ph–P=O locking unit. The D-NBNPS device demonstrates better performances with an EQE$_{max}$ of 31.6%, a CE$_{max}$ of 35.8 cd A^{-2} and a PE$_{max}$ of 28.8 lm W^{-1}, respectively, and the efficiency roll-off is significantly suppressed compared to that of D-NBNPO. At a luminance of 100 and 1000 cd m^{-2}, the EQEs are comparative with values of 20.9% and 19.5%, respectively. Even at a high brightness of 2000, 3000, and 4000 cd m^{-2}, the EQEs remain at 19.4%, 17.7%, and 16.5%, respectively. These results suggest that the introduction of the Ph–P=S lock in the MR framework is beneficial for an efficient device with low efficiency roll-off. However, compared to D-NBNPO and D-NBNPS, the EQE$_{max}$ of D-NBNPSe decreases to 11.4%, which correlates with the intrinsically low Φ_{PL} (61%) of NBNPSe. But notably, the D-NBNPSe device demonstrates a significantly reduced efficiency roll-off. From the maximum value to a brightness of 1000 cd m^{-2}, the EQEs are around 11%. At a high brightness of 2000, 3000, and 4000 cd m^{-2}, the EQEs remain at 10.5%, 9.0%, and 7.8%, respectively. We believe that the rigid molecular structure with a short delayed lifetime (2.93 μs) of NBNPSe is responsible for this phenomenon (Table 2). Although the incorporation of a Se atom in the emitter leads to a decrease in the peak efficiency of its device, it plays a pivotal role in enhancing device stability. These findings also highlight the potential and challenge of heavy atom integration in achieving a balanced trade-off between efficiency and roll-off in future MR-TADF materials and OLED design.

Table 2 EL performance data of TADF sensitized OLEDs

Device	$V_{turn\text{-}on}$[a] [V]	λ_{EL}[b] [nm]	FWHM [nm eV^{-1}]	CIE [x, y]	L_{max}[c] [cd m^{-2}]	CE$_{max/100/1000}$[d] [cd A^{-1}]	EQE$_{max/100/1000}$[e] [%]	PE$_{max}$[f] [lm W^{-1}]
D-NBNPO	3.9	467	22/0.13	0.12, 0.09	8040	34.67/18.77/15.66	32.4/17.6/14.7	25.9/10.5/6.6
D-NBNPS	3.8	472	27/0.15	0.11, 0.12	14 883	35.83/23.73/22.08	31.6/20.9/19.5	28.8/14.3/10.9
D-NBNPSe	4.0	472	33/0.18	0.12, 0.13	6670	11.47/10.33/11.36	11.2/10.2/11.1	8.7/5.1/4.8

[a] Turn on voltage recorded at a brightness of 1 cd m^{-2}. [b] Electroluminescence peak at 7 V. [c] Maximum luminance. [d] Maximum power efficiency, measured at luminance levels of 1000/10000 cd m^{-2}. [e] Maximum external quantum efficiency and external quantum efficiency measured at 100 and 1000 cd m^{-2}. [f] Maximum power efficiency.

Conclusions

In conclusion, this work presents a heavy-atom-assisted phenylphosphine locking strategy by introducing functional Ph–P=X units (X = O, S, Se) into a DtCzB-based MR framework. This design synergistically enhances molecular rigidity and SOC, significantly accelerating the RISC process while preserving the characteristic narrowband emission of MR-TADF materials, ultimately contributing to good photophysical properties. As a result, NBNPO, NBNPS, and NBNPSe emitters exhibit blue emission with peak wavelengths of 468, 471, and 471 nm as well as FWHMs of 19 (0.11 eV), 19 (0.11 eV), and 27 nm (0.15 eV), respectively. Thanks to the heavy atom effect, the k_{RISC} values were determined to be 5.92×10^4, 4.62×10^5, and 9.91×10^6 s^{-1} for NBNPO, NBNPS, and NBNPSe, respectively. The corresponding sensitized OLEDs based on NBNPO, NBNPS, and NBNPSe demonstrate $\mathrm{EQE}_{\max}$ values of 32.4%, 31.6%, and 11.4%, with a gradual reduction in efficiency roll-off. These results underscore the importance of rationally designing molecular structures and controlling heavy atom effects to balance the trade-off between high efficiency and minimal efficiency roll-off, thereby guiding future advancements in MR-TADF material design for OLED application.

Author contributions

X.-F. Hong: conceptualization, data curation, formal analysis, investigation, methodology, visualization, writing – original draft. Y. Wei: investigation, project administration. H.-R. Xing: investigation, software. Y. Wang: project administration, software. J.-Q. Xi: project administration, validation. C.-Y. Wu: investigation, methodology. L. Yuan: investigation, writing – review & editing. C.-H. Li: conceptualization, project administration, supervision. Y. X. Zheng: conceptualization, funding acquisition, project administration, supervision, writing – review & editing.

Conflicts of interest

The authors declare no conflict of interest.

Data availability

The datasets generated or analyzed during the current study will be available from the corresponding author on reasonable request.

CCDC 2452670–2452672 contain the supplementary crystallographic data for this paper.[48a–c]

Supplementary information: the general information for the reagents for the compound synthesis and measurement, the synthesis and characterization (^{1}H NMR and ^{13}C NMR spectra, high-resolution mass spectrometry, thermogravimetric analysis and cyclic voltammogram curves, single-crystal structures, transient PL prompt and decay curves), theoretical calculation results, normalized PL spectra in doped films of three materials, device architecture, molecular structures of materials and device performances of the unoptimized OLEDs, normalized EL spectra at different voltage of sensitized devices. See DOI: https://doi.org/10.1039/d5sc06565h.

Acknowledgements

This work was supported by the Natural Science Foundation of Jiangsu Province (BK20243010, BK20242021, and BK20251239), China Postdoctoral Science Foundation (2024M761379) and Jiangsu Funding Program for Excellent Postdoctoral Talent (2025ZB414).

Notes and references

1 T. Hatakeyama, K. Shiren, K. Nakajima, S. Nomura, S. Nakatsuka, K. Kinoshita, J. Ni, Y. Ono and T. Ikuta, *Adv. Mater.*, 2016, **28**, 2777.
2 M. Hayakawa, X. Tang, Y. Ueda, H. Eguchi, M. Kondo, S. Oda, X.-C. Fan, G. N. Iswara Lestanto, C. Adachi and T. Hatakeyama, *J. Am. Chem. Soc.*, 2024, **146**, 18331.
3 X.-F. Luo, S.-Q. Song, H.-X. Ni, H. Ma, D. Yang, D. Ma, Y.-X. Zheng and J.-L. Zuo, *Angew. Chem., Int. Ed.*, 2022, **61**, e202209984.
4 T. Fan, M. Du, X. Jia, L. Wang, Z. Yin, Y. Shu, Y. Zhang, J. Wei, D. Zhang and L. Duan, *Adv. Mater.*, 2023, **35**, 2301018.
5 X. Liang, Z.-P. Yan, H.-B. Han, Z.-G. Wu, Y.-X. Zheng, H. Meng, J.-L. Zuo and W. Huang, *Angew. Chem., Int. Ed.*, 2018, **57**, 11316.
6 M. Yang, I. S. Park and T. Yasuda, *J. Am. Chem. Soc.*, 2020, **142**, 19468.
7 Y. Xu, Z. Cheng, Z. Li, B. Liang, J. Wang, J. Wei, Z. Zhang and Y. Wang, *Adv. Opt. Mater.*, 2020, **8**, 1902142.
8 Y. Zhang, D. Zhang, J. Wei, Z. Liu, Y. Lu and L. Duan, *Angew. Chem., Int. Ed.*, 2019, **58**, 16912.
9 Y. Xu, C. Li, Z. Li, J. Wang, J. Xue, Q. Wang, X. Cai and Y. Wang, *CCS Chem.*, 2022, **4**, 2065.
10 M. Yang, R. K. Konidena, S. Shikita and T. Yasuda, *J. Mater. Chem. C*, 2023, **11**, 917.
11 X. Cai, Y. Xu, Y. Pan, L. Li, Y. Pu, X. Zhuang, C. Li and Y. Wang, *Angew. Chem., Int. Ed.*, 2023, **62**, e202216473.
12 D. Chen, H. Wang, D. Sun, S. Wu, K. Wang, X.-H. Zhang and E. Zysman-Colman, *Adv. Mater.*, 2024, **36**, 2412761.
13 Y. Hu, J. Miao, C. Zhong, Y. Zeng, S. Gong, X. Cao, X. Zhou, Y. Gu and C. Yang, *Angew. Chem., Int. Ed.*, 2023, **62**, e202302478.
14 X.-J. Liao, D. Pu, L. Yuan, J. Tong, S. Xing, Z.-L. Tu, J.-L. Zuo, W.-H. Zheng and Y.-X. Zheng, *Angew. Chem., Int. Ed.*, 2023, **62**, e202217045.
15 Y. Xu, Q. Wang, X. Cai, C. Li and Y. Wang, *Adv. Mater.*, 2021, **33**, 2100652.
16 G. Meng, H. Dai, J. Zhou, T. Huang, X. Zeng, Q. Wang, X. Wang, Y. Zhang, T. Fan, D. Yang, D. Ma, D. Zhang and L. Duan, *Chem. Sci.*, 2023, **14**, 979.
17 M. Yang, S. Shikita, H. Min, I. S. Park, H. Shibata, N. Amanokura and T. Yasuda, *Angew. Chem., Int. Ed.*, 2021, **60**, 23142.
18 K. R. Naveen, S. J. Hwang, H. Lee and J. H. Kwon, *Adv. Electron Mater.*, 2021, **8**, 2101114.

19 Y.-H. He, F.-M. Xie, H.-Z. Li, K. Zhang, Y. Shen, F. Ding, C.-Y. Wang, Y.-Q. Li and J.-X. Tang, *Mater. Chem. Front.*, 2023, **7**, 2454.

20 H. L. Lee, S. O. Jeon, I. Kim, S. C. Kim, J. Lim, J. Kim, S. Park, J. Chwae, W. J. Son, H. Choi and J. Y. Lee, *Adv. Mater.*, 2022, **34**, 2202464.

21 J. Liu, Y. Zhu, T. Tsuboi, C. Deng, W. Lou, D. Wang, T. Liu and Q. Zhang, *Nat. Commun.*, 2022, **13**, 4876.

22 X. Wang, L. Wang, G. Meng, X. Zeng, D. Zhang and L. Duan, *Sci. Adv.*, 2023, **9**, eadh1434.

23 Y. Pu, Q. Jin, Y. Zhang, C. Li, L. Duan and Y. Wang, *Nat. Commun.*, 2025, **16**, 332.

24 Y. Pu, X. Cai, Y. Qu, W. Cui, L. Li, C. Li, Y. Zhang and Y. Wang, *Angew. Chem., Int. Ed.*, 2024, **64**, e202420253.

25 L. Xing, J. Wang, W.-C. Chen, B. Liu, G. Chen, X. Wang, J.-H. Tan, S. S. Chen, J.-X. Chen, S. Ji, Z. Zhao, M.-C. Tang and Y. Huo, *Nat. Commun.*, 2024, **15**, 6175.

26 X.-J. Liao, S. Xing, J.-J. Hu, X.-Z. Wang and Y.-X. Zheng, *CCS Chem.*, 2025, **7**, 2419–2431.

27 Y. Wang, Z.-Y. Lv, Z.-X. Chen, S. Xing, Z.-Z. Huo, X.-F. Hong, L. Yuan, W. Li and Y.-X. Zheng, *Mater. Horiz.*, 2024, **11**, 4722.

28 Z. Liu, L. Meng, Y. Jiang, C. Li, H. Gu, K. Zhao, J. Zhang, H. Meng and Y. Ren, *J. Am. Chem. Soc.*, 2025, **147**, 3650.

29 J. Bian, S. Chen, L. Qiu, R. Tian, Y. Man, Y. Wang, S. Chen, J. Zhang, C. Duan, C. Han and H. Xu, *Adv. Mater.*, 2022, **34**, 2110547.

30 X. Xiong, J.-Q. Li, T.-F. Chen, X.-C. Fan, Y.-C. Cheng, H. Wang, F. Huang, H. Wu, J. Yu, X.-K. Chen, K. Wang and X.-H. Zhang, *Adv. Funct. Mater.*, 2024, **34**, 2313726.

31 Z. Liu, I. S. Park, H. Min and T. Yasuda, *Angew. Chem., Int. Ed.*, 2022, **61**, e202205684.

32 Y. X. Hu, J. Miao, T. Hua, Z. Huang, Y. Qi, Y. Zou, Y. Qiu, H. Xia, H. Liu, X. Cao and C. Yang, *Nat. Photonics*, 2022, **16**, 803.

33 P. Ma, Y. Chen, Y. Man, Q. Qi, Y. Guo, H. Wang, Z. Li, P. Chang, C. Qu, C. Han and H. Xu, *Angew. Chem., Int. Ed.*, 2023, **63**, e202316479.

34 J. Dong, Y. Xu, S. Wang, J. Miao, N. Li, Z. Huang and C. Yang, *Chem. Commun.*, 2024, **60**, 6789.

35 S. Chen, Y. Wang, J. Lin, R. Tian, S. Li, Y. Man, S. Chen, J. Zhang, C. Duan, C. Han and H. Xu, *Chem. Eng. J.*, 2024, **489**, 151517.

36 X. Cao, K. Pan, J. Miao, X. Lv, Z. Huang, F. Ni, X. Yin, Y. Wei and C. Yang, *J. Am. Chem. Soc.*, 2022, **144**, 22976.

37 Z. Chen, D. Liu, M. Li, Y. Jiao, Z. Yang, K. Liu and S. J. Su, *Adv. Funct. Mater.*, 2024, **34**, 2404278.

38 Q. Zheng, Y.-K. Qu, P. Zuo, H.-T. Yuan, Y.-J. Yang, Y.-C. Qiu, L.-S. Liao, D.-Y. Zhou and Z.-Q. Jiang, *Chem*, 2025, **11**, 102353.

39 J. Szumilas, C. H. Ryoo, M. Mońka, P. Bojarski, S. Y. Park and I. E. Serdiuk, *J. Mater. Chem. C*, 2025, **13**, 8043.

40 S. K. Lower and M. A. El-Sayed, *Chem. Rev.*, 1966, **66**, 199.

41 M. Rae, F. Perez-Balderas, C. Baleizão, A. Fedorov, J. A. S. Cavaleiro, A. C. Tomé and M. N. Berberan-Santos, *J. Phys. Chem. B*, 2006, **110**, 12809.

42 J. Xu, X. Wu, J. Li, Z. Zhao and B. Z. Tang, *Adv. Opt. Mater.*, 2022, **10**, 2102568.

43 S. O. Jeon, K. H. Lee, J. S. Kim, S.-G. Ihn, Y. S. Chung, J. W. Kim, H. Lee, S. Kim, H. Choi and J. Y. Lee, *Nat. Photonics*, 2021, **15**, 208.

44 C.-Y. Chan, M. Tanaka, Y.-T. Lee, Y.-W. Wong, H. Nakanotani, T. Hatakeyama and C. Adachi, *Nat. Photonics*, 2021, **15**, 203.

45 D. Zhang, X. Song, A. J. Gillett, B. H. Drummond, S. T. E. Jones, G. Li, H. He, M. Cai, D. Credgington and L. Duan, *Adv. Mater.*, 2020, **32**, 1908355.

46 R. Braveenth, H. Lee, J. D. Park, K. J. Yang, S. J. Hwang, K. R. Naveen, R. Lampande and J. H. Kwon, *Adv. Funct. Mater.*, 2021, **31**, 2105805.

47 T. Huang, Q. Wang, H. Zhang, Y. Xin, Y. Zhang, X. Chen, D. Zhang and L. Duan, *Nat. Mater.*, 2024, **23**, 1523.

48 (*a*) CCDC 2452670: Experimental Crystal Structure Determination, 2025, DOI: **10.5517/ccdc.csd.cc2nb6dm**; (*b*) CCDC 2452671: Experimental Crystal Structure Determination, 2025, DOI: **10.5517/ccdc.csd.cc2nb6fn**; (*c*) CCDC 2452672: Experimental Crystal Structure Determination, 2025, DOI: **10.5517/ccdc.csd.cc2nb6gp**.